Analysis of an Nth-order nonlinear differential-delay equation

Réal Vallée and Christopher Marriott
Laboratoire de Recherches en Optique et Laser, Département de Physique, Université Laval, Sainte Foy, Canada G1K 7P4
(Received 6 July 1988)

The problem of a nonlinear dynamical system with delay and an overall response time which is distributed among N individual components is analyzed. Such a system can generally be modeled by an Nth-order nonlinear differential delay equation. A linear-stability analysis as well as a numerical simulation of that equation are performed and a comparison is made with the experimental results. Finally, a parallel is established between the first-order differential equation with delay and the Nth-order differential equation without delay.

I. INTRODUCTION

Self-oscillating and chaotic behavior in dynamical systems has been the subject of recent investigations. In optical bistability, since the work of Ikeda,[1] a good deal of interest has been focused on hybrid devices as simple and reliable models for the study of instabilities in delay-differential systems. Among the problems connected with these systems, the question of the relevance of the corresponding discrete model to describing the dynamical evolution toward chaos as a control parameter is varied has been thoroughly debated. In particular, the situation characterized by a large ratio of the delay τ_d to the total response time τ led Ikeda in his early model to make the adiabatic elimination assumption which has been questioned recently.[2] Actually, such an elimination would be appropriate in the case of a system with no delay but with two (or many) response times when one is much larger than the other(s). However, in the situation where a delay and a single response time are involved the response time cannot be neglected because of the transient effects occurring on this time scale. This is especially true in the chaotic regime where an increase in the complexity of the solutions must be expected as the ratio τ_d/τ is increased.

In a recent paper[3] it was shown that a hybrid bistable device can generally be described by an Nth-order differential-delay equation when N independent components contribute to the total response time. In particular, the case $N=2$ was analyzed and it was shown that the second-order differential term explains the discrepancies observed between the numerical and experimental results when the delay is of the same or smaller order than the total response time. Here we analyze the general case of N independent response times which give rise to the Nth-order differential-delay equation:

$$\prod_{i=1}^{N}\tau_i\frac{d^N X(t)}{dt^N}+\cdots+\sum_{i=1}^{N}\sum_{j>i}^{N}\sum_{k>j}^{N}\tau_i\tau_j\tau_k\frac{d^3X(t)}{dt^3}+\sum_{i=1}^{N}\sum_{j>i}^{N}\tau_i\tau_j\frac{d^2X(t)}{dt^2}+\sum_{i=1}^{N}\tau_i\frac{dX(t)}{dt}+X(t)=F(X(t-\tau_d);\mu)\ , \tag{1}$$

where $\tau=\sum_i\tau_i$, $F(X(t-\tau_d))$ is a nonlinear function, μ the control parameter, and τ_d the time lag. In the case of the acoustooptic device one has

$$F(X(t-\tau_d);\mu)=\pi\{A-\mu\sin^2[X(t-\tau_d)-X_B]\}\ . \tag{2}$$

A special case which can be considered without too much loss of generality consists in equating the individual response times τ_i to the same value τ/N so that Eq. (1) becomes

$$\sum_{m=0}^{N}\left[\frac{\tau}{N}\right]^m C_m^N X^{(m)}=F(X(t-\tau_d);\mu)\ , \tag{3}$$

where $X^{(m)}$ is the mth derivative of $X(t)$ and C_m^N represents the number of combinations of N quantities taken m at a time.

As will be shown below the interest in studying the Nth-order equation arises from the fact that for $N\geq 3$ self-oscillation becomes possible even for a delay equal to zero—which does not occur for the first- or second-order equation. In the particular case ($\tau_d=0$) which will be discussed at length here, the resulting Nth-order differential equation describes a system having a finite number (namely, N) of degrees of freedom. Therefore it becomes possible to study the dynamical evolution of the system as a function of N and μ in the same manner as a first-order differential-delay equation can be analyzed as a function of τ_d/τ and μ. In fact, a correspondence between the two systems will be established in Sec. IV. Beforehand, results of a linear-stability analysis (in Sec. II A) and of a numerical simulation (Sec. II B) of Eq. (3) will be shown. The experimental results will be presented in Sec. III.

II. ANALYSIS

A. Linear-stability analysis

The linear-stability analysis[3,4] of Eq. (3) leads in a straightforward manner to the Nth-degree equation

$$\sum_{m=0}^{N} K_m \gamma^m + Be^{-\gamma\tau_d} = 0 , \tag{4}$$

where

$$K_m = \left[\frac{\tau}{N}\right]^m C_m^N , \tag{5}$$

$$B = -\left.\frac{dF}{dX}\right|_{X=X^*} , \tag{6}$$

and $\gamma \equiv \alpha + j\beta$. The N solutions γ_i can be obtained by solving Eq. (4) in the complex plane. Each solution corresponds to a linear mode in the system whose natural frequency of oscillation is given by β_i. The real part α_i is an attenuation (or amplification) factor. Now, since the situation $\alpha_i \geq 0$ implies the instability of the fixed point solution of the ith mode, its threshold of self-oscillation can be obtained as a function of N and τ_d/τ by putting $\alpha_i = 0$. Result of such an analysis for the first linear mode to become unstable ($i = 1$) are shown in Fig. 1. It appears that the asymptotic behavior for $\tau_d/\tau \to \infty$ is the same for all N, i.e., the thresholds of self-oscillation tend toward the lower limit predicted by the discrete model (0.324...). However, for $\tau_d/\tau \to 0$ the self-oscillation thresholds strongly depend on N. For $N \leq 2$ the threshold goes to infinity as τ_d/τ is decreased. For $N = 3$, however, the threshold reaches an upper limit equal to 6.02..., which means that self-oscillation is now possible for a delay τ_d strictly equal to zero. This upper limit rapidly decreases with N increasing so that for large N (typically $N > 20$) the bifurcation point is almost independent of the ratio τ_d/τ and equal to the discrete model value. The last result should not be surprising since it can be derived directly from Eq. (4). The summation term in (4) can be written

$$\sum_{m=0}^{N} \left[\frac{\gamma\tau}{N}\right]^m C_m^N = \left[1 + \frac{\gamma\tau}{N}\right]^N , \tag{7}$$

which tends toward $e^{\gamma\tau}$ for N large. Therefore Eq. (4) can be written in the asymptotic case defined by $N \to \infty$:

$$Be^{-\gamma(\tau_d+\tau)} = -1 , \tag{8}$$

from which we obtain for $\alpha = 0$:

$$\beta(\tau_d + \tau) = k\pi \quad (k \text{ odd}) , \tag{9a}$$

$$B = +1 , \tag{9b}$$

where the minus sign is rejected in (9b)—because the function $F(X)$ has a negative slope at the fixed point of interest—and therefore k must be odd. This result tells us that as N is increased the slope of the nonlinear function $F(X)$ at the fixed point approaches -1 at the onset of the self-oscillation, as in the case of the corresponding difference equation (discrete model). It also appears that the period of the self-oscillation corresponding to the first linear mode ($k = 1$) is given by $2(\tau_d + \tau)$, regardless of the ratio τ_d/τ. The first mode, because it is the first to become unstable, plays a dominant role in the dynamics of the system, especially for $N < 50$. It is to be remarked that a similar case of mode hierarchy is observed in the first-order differential-delay equation.[4,5] In both cases, as N (or τ_d/τ in the first-order case) is increased, the frequencies of the higher modes approach the frequencies of the odd harmonics of the first mode.

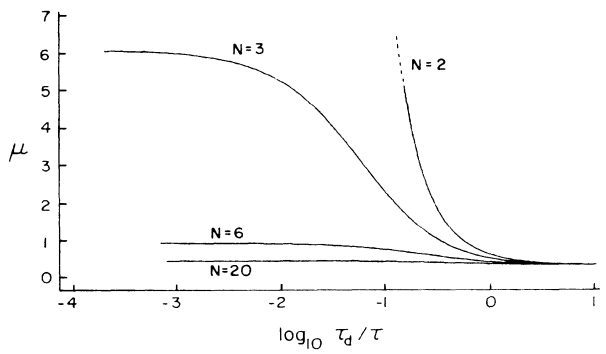

FIG. 1. Thresholds of self-oscillation for various values of N.

B. Numerical simulation

To proceed with the numerical integration of the Nth-order differential-delay equation one must first transform it into a system of N first-order differential-delay equations. When N is large special care must be taken to avoid divergence of the solution. This can be easily understood, as for a simple harmonic signal $\sin(\omega t)$ the mth derivative is proportional to ω^m. Fortunately the coefficient (hereafter defined as C_m to shorten the notation) appearing in front of the $(m-1)$th derivative in Eq. (1) compensates for the growth of the latter. This naturally suggests the following definition for the variable u_m used in the computation:

$$u_m = C_m X^{(m-1)} . \tag{10}$$

With this definition Eq. (1) can be rewritten in terms of a set of N equations:

$$\begin{aligned} \dot{u}_m &= \left[\frac{c_1}{c_2}\right] u_{m+1} \quad (m = 1,2,\ldots,N-1) , \\ \dot{u}_N &= \left[\frac{c_N}{c_{N+1}}\right] \{F(u_1) - u_1 - u_2 - \cdots - u_N\} . \end{aligned} \tag{11}$$

This set of equations can be easily integrated using a Runge-Kutta algorithm[6] generalized to a system of first-order equations. We were able to integrate Eq. (1) in this manner for N as large as 110. Naturally the usual tests to ensure the exactness of the simulation were performed; the comparison with the experimental results being the ultimate one. Notice that the preceding definition of u_m is not necessary but was chosen to avoid the overflow problems which occur with the more natural definition $u_m = X^{(m)}$. In fact, using this definition in our first at-

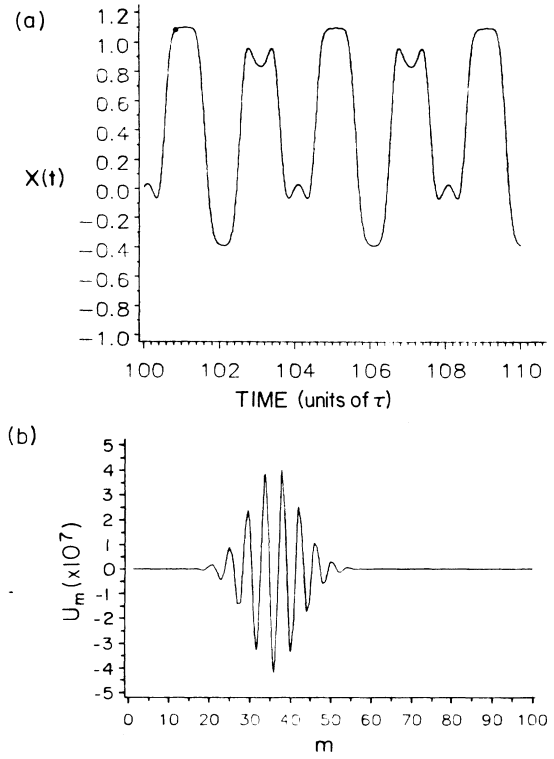

FIG. 2. Solution of Eq. (3) for $N=100$, $\tau_d=0$, $A=0.35$, $X_B=0$, and $\mu=0.6$. The dot indicates the point for which the sequence of parameters u_m has been plotted in (b). The parameters u_m are joined by straight lines.

tempt we were limited to values of N less than 45.

The compensation between the derivatives and their coefficients takes a peculiar form, as is shown in Fig. 2(b), where u_m has been plotted as a function of m. It appears that although the parameter u_m can take on very large values around $m=35$ its average value is on the order of unity, which ensures the stability of the solution. Moreover, various tests for various states of the solution have shown that the envelope of the coefficients usually shows a single bell-like structure. We also noticed that even if the amplitude and the shape of the envelope could change significantly with the step size h used in the computation, the resulting temporal solution for $X(t)$ [Fig. 2(a)] remained unchanged. A test of the resolution of the computation was performed by computing the standard deviation between solutions obtained with different h using the most precise solution as the reference. A log-log plot of these standard deviations as a function of h showed a slope of about 2.5, which indicates that the numerical error increases as $h^{2.5}$. This compares with the nominal error of the Runge-Kutta algorithm used (h^3).

III. RESULTS

A. Experiment

The basic acoustooptic hybrid bistable device (HBD) used in this experiment has been described elsewhere.[7] The main modification to this setup was the introduction in the feedback loop of a series of RC circuits each separated from its neighbor by an isolation stage of unitary gain. The nominal values of the electronic components were the same at each stage so that the unavoidable fluctuation in the values of the resulting response times was on the order of $\pm 10\%$. The value of the intrinsic delay was always very close to the zero delay limit (τ_d/τ less than 10^{-3} in most cases). The parameters A and X_B were fixed to 0.35 and zero, respectively. Experimental bifurcation diagrams showing the dynamical evolution of the system as a function of μ for N varying from 3 to 35 were obtained by electronically detecting the zeros of the first derivative of $X(t)$ while the control parameter μ was swept by the use of a second acoustooptic modulator (see Ref. 7). (Notice that similar results are obtained when the zeros of the higher-order derivatives are considered.) Our experimental results are summarized in Fig. 3.

For $N=4$ a Hopf bifurcation occurs for $\mu \approx 2.0$ but the system never undergoes subsequent period-doubling bifurcations and it remains in the period-2 ($P2$) state until it precipitates for $\mu \approx 5.5$. This precipitation occurs as the system switches to its stable lower bistability branch. For $N=5$ a sudden transition occurring with hysteresis is observed around $\mu=3.2$. This transition results in changes in the shape and the period of the temporal signal. It is interesting to note that, while the first of these signals clearly corresponds to the $P2$ waveform (since its period is very close to 2τ) the second one (after the jump) could probably be associated with the $P3$ waveform even though its period is not quite equal to 3τ. For N ranging from 6 to 8 a "period bubbling"[8] of the solutions is observed such that the $P4$ oscillation eventually returns to the $P2$ waveform. For $N=9$ a chaotic solution is reached through a probably infinite period-doubling sequence. But instead of presenting the usual inverse Lorenz sequence the system undergoes an inverse period-doubling sequence such that the $P2$ waveform reappears for $\mu > 1.8$. For $N=10$ a crisis occurs at $\mu=1.8$, which results in the onset of a chaotic solution associated with a $P3$ mapping process. A backward sweep of μ shows a hysteresis of the solution around this transition and therefore clearly indicates the existence of two attractors. Poincaré sections of these chaotic attractors also confirm the two-attractor hypothesis. A $P3$ waveform appears following a crisis for $N=11$. The temporal shape of this waveform as shown at Fig. 4(a) explains why it appears as a four-branched attractor in the photograph. In fact, the appearance of the $P3$ waveform seems to be related to the median overshoot of the solution which already exists in the chaotic-2 ($C2$) region. This overshoot shows up in the growth of a triangle for N ranging from 12 to 15 and its spreading, as μ is increased, is responsible for the progressive filling up of the "forbidden band" (around $X=0.4$) between the two branches of the $C2$ attractor. A bend of the $P4$ interior branches begins to be observed for $N=15$, gradually becoming sharper until it eventually results in a crisis at $N=18$ ($\mu=1.13$) characterized by a transition from $P4$ to chaos. The same crisis is observed for $N=19$ and 20 but it is now preceded by a "bubbling" of the $P8$ waveform. It is

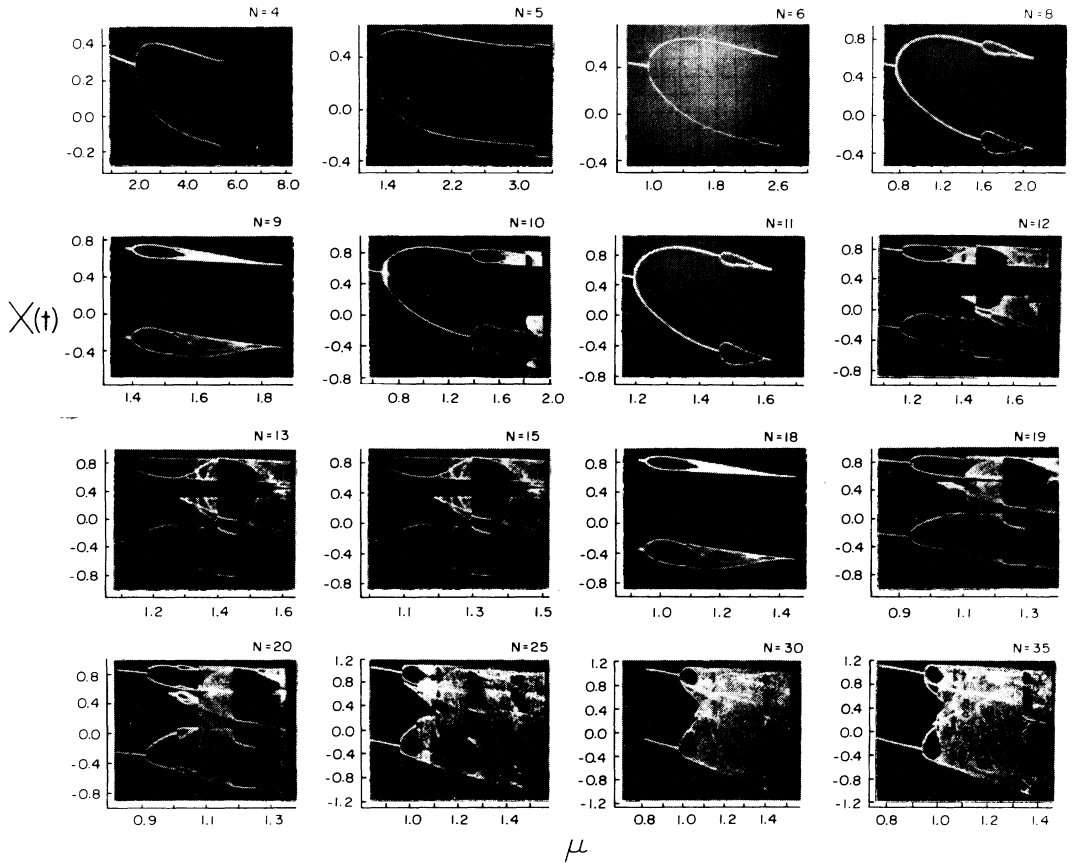

FIG. 3. Experimental bifurcation diagrams.

also interesting to note that for $N=20$ the transition to the $P3$ waveform looks like a tangent bifurcation and that the width of the corresponding window is unusually wide. For $N=25$, the onset of chaos returns to normal (i.e., through a period-doubling sequence); meanwhile, the $P3$ window has been noticeably shrunk. The $P3$ waveform has completely disappeared for $N=30$. It is also to be noticed that the veil-like structure on the diagrams increasingly blurred as N is increased. The periodic windows appearing within the chaotic region for $N=30$ and 35 correspond to the two $P5$ waveforms shown on Figs. 4(b) and 4(c).

From the preceding results it is clear that the increasing complexity of the solutions is probably the most striking effect to be observed in the system as N is increased. The first step of this increase in complexity, the onset of self-oscillation, was correctly predicted by the linear-stability analysis to occur for $N=3$. However, an exhaustive analysis of the system for different settings of the relevant parameters has shown to us that although the sequence of events was rather unique the value of N at which a specific phenomenon was occurring could vary. For instance, the first onset of a chaotic solution does not depend on μ and N only and is therefore not fixed to $N=9$. As a matter of fact, for other values of A and X_B chaotic solutions were observed only for $N \geq 11$. In fact, the smallest value for which one could clearly observe chaotic solutions was $N=8$ (for $A=0.35$, $X_B=0$) when care was taken to equalize as much as possible the individual response times. Therefore the importance of the preceding results is not so much in the specific values of N for which the phenomena occur but in the sequence in which they appear. This fact will become more obvious after the comparison is made with the numerical results.

B. Numerical analysis

Results of the numerical analysis are summarized in Fig. 5. The agreement with the experimental results is almost perfect as far as the sequence (as N is increased) of bifurcation diagrams is concerned. However, one can see a discrepancy between the values of N for which a specific bifurcation diagram is obtained experimentally and numerically. For instance, the diagram computed for $N=17$ would correspond, apart from a shift of the parameter μ, to what is observed experimentally for $N=20$.

After an analysis of the influence of the various parameters we found that the discrepancy is related to the small but unavoidable inequality between the individual response times in the experiment which are assumed strictly equal in the computations. We therefore pro-

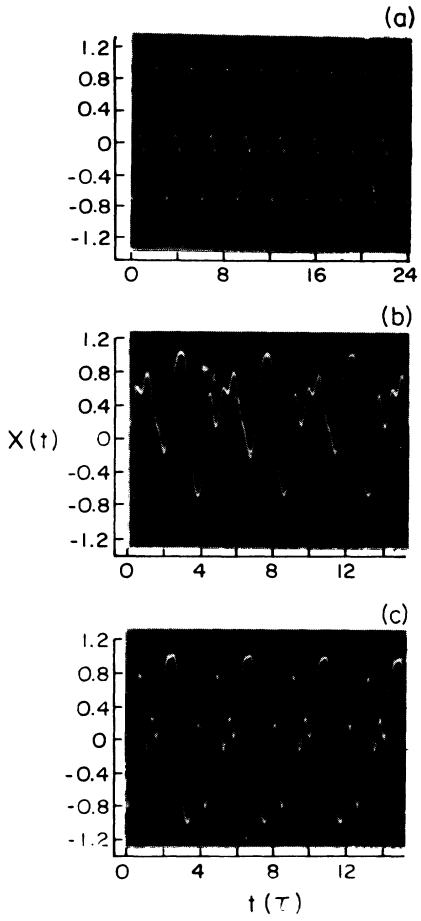

FIG. 4. Periodic waveforms: (a) $P3$ as observed for $N=15$ and $\mu\approx 1.35$; (b) $P5$ for $N=35$ and $\mu=1.07$; (c) $P5$ for $N=35$ and $\mu=1.33$.

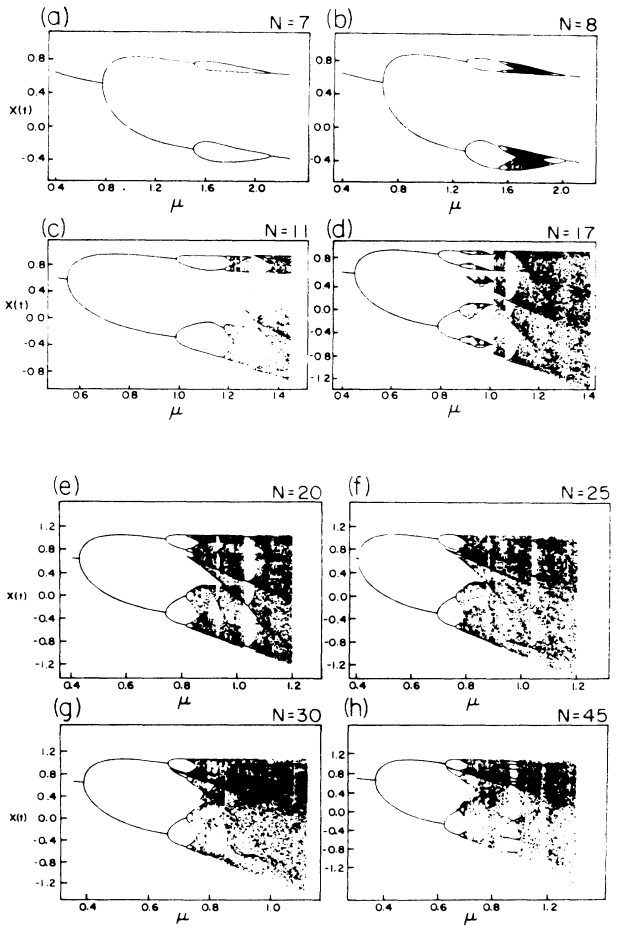

FIG. 5. Numerical bifurcation diagrams for various N ($\tau_d/\tau=0$). Points of these diagrams correspond to zeros of the first derivative of $X(t)$.

ceeded with a simple test consisting of using the actual experimental values of the individual response times in the computation of the coefficients of Eq. (1). The results for $N=20$ (shown in Fig. 6) are conclusive as an almost perfect qualitative (shape of the diagram) agreement is observed between the experimental and computed diagrams. In this example the relative standard deviation of the τ_i was 9% and observable changes were produced (cf. Fig. 5 for $N=20$). However, for smaller relative standard deviations (around 5%) the effects were barely noticeable. It should also be pointed out that the results shown in Fig. 5 were obtained for $\tau_d=0$, although an unavoidable intrinsic delay was always present in the experimental device. In fact, it is clear from Fig. 1 that as τ_d is decreased the self-oscillation thresholds asymptote towards a fixed value. However, this analysis is applicable only to the fixed point stability. This is why we proceeded to an investigation of the solution of the Nth-order differential equation with delay in order to estimate the influence of the nonzero delay on the subsequent period-doubling route to chaos. Typical results are shown for $N=8$ in Figs. 7(a)–7(c). For small values of τ_d/τ (typically less than 10^{-3}) Fig. 7(a) shows no observable difference when compared with the no delay case (cf. Fig. 5). (This is especially fortunate for very short delays, as it allowed us to model the experimental system by the ordinary differential equation without delay [Eq. (1) with $\tau_d=0$]. This considerably reduced the computation time, since in the case with delay, it is necessary to have at least one point for every delay interval. Thus the maximum value of the step size h is fixed by τ_d. With $\tau_d/\tau=10^{-4}$, for instance, the maximum value for h would be 10^{-4} (in units of τ), which implies that the number of points per oscillation period [approximately $2(\tau+\tau_d)$] is around $2\times 10^{+4}$. On the other hand, by integrating the ordinary differential equation without delay similar results were obtained with only 500 points per oscillation period.) The changes introduced by a nonzero delay become obvious for τ_d/τ larger than 10^{-1} [Fig. 7(b)], as if a nonzero delay corresponds to an increase in the order of the equation. Further increasing τ_d/τ leads us to results which approach what is observed for the more familiar first-order delay-differential equation case [Figs. 7(c) and (d)].

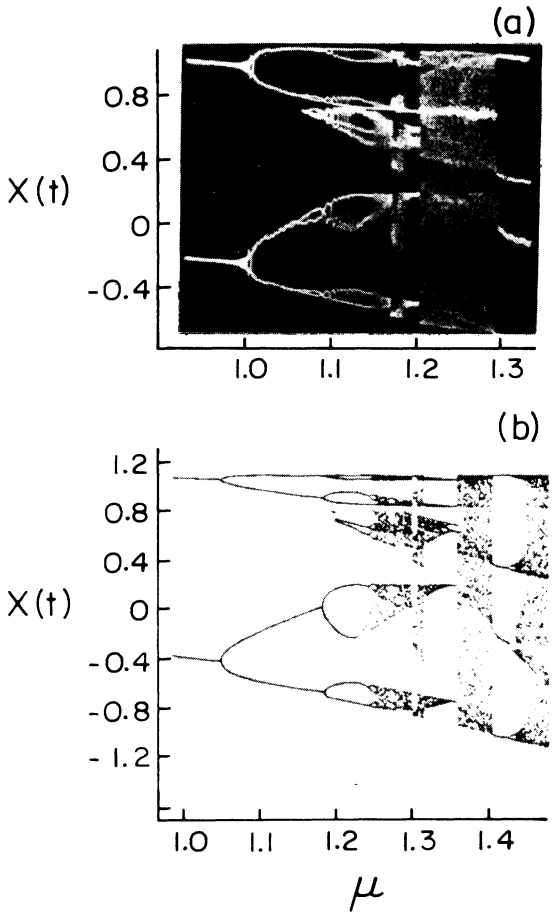

FIG. 6. Comparison between the experimental (a) and the numerical (b) bifurcation diagrams obtained for $N=20$ using the experimental values of τ_i in the computation.

The numerical simulation also allowed us to extend our analysis of the system up to $N=100$, which for practical reasons is not possible in the experimental device. Very interesting results were found within the range $50<N<100$ which revealed the presence of the second linear mode. The bifurcation diagrams computed for $N=100$ are shown in Fig. 8. The wide periodic window appearing on this diagram for μ ranging from 0.8 to 0.975 is associated with a fundamental oscillation of frequency equal to three times that of the $P2$ waveform. This oscillation clearly corresponds to the $P2$ waveform of the second linear mode of the system or—according to a previously defined notation[9]—to the $^2P2$ waveform. As μ is increased beyond 0.975 the $^2P2$ waveform bifurcates towards as two-attractor solution. In fact, in the interval $0.975<\mu<1.015$ two distinct oscillating solutions (or branches) can be reached depending on the initial conditions used in the computations [Figs. 8(b) and 8(c)]. The first solution consists of the sequence of subharmonics of $^2P2$ resulting from successive period-doubling bifurcations with an accumulation point around 1.02 [Fig. 8(c)]. In Fig. 8(b) this solution shows up as a small window for $\mu>1.015$. The time signal as well as the fast Fourier transform of the $^2P16$ waveform are shown in Figs. 9(d) and 9(e). The second solution, which is the most readily attainable of the two, appears in the interval $0.98<\mu<1.015$ of Fig. 8(b). This solution corresponds to a state in which the first two modes of the system interact. This interaction occurs between the $^2P2$ waveform and a frequency component related to $P4$ (the $P4$ waveform of the first mode) which is near $(\frac{2}{11})$ the frequency of the $^2P2$ oscillation. In fact, this solution is

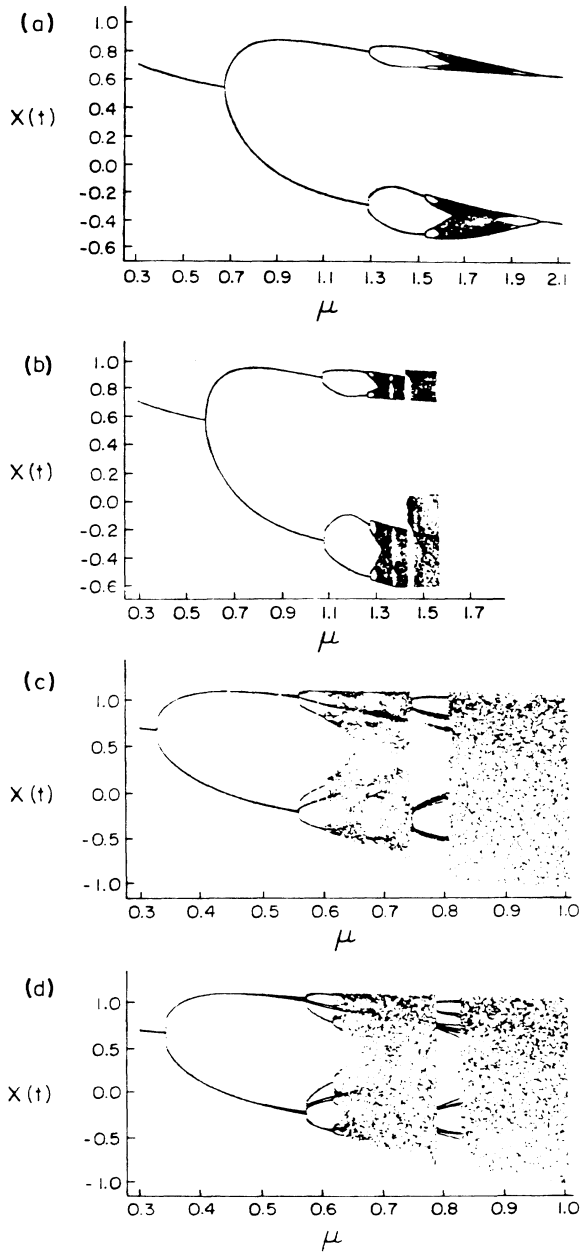

FIG. 7. Numerical bifurcation diagrams for $N=8$ and three values of the ratio τ_d/τ: (a) 10^{-3}; (b) 10^{-1}; (c) 10. In (d) the diagram for $N=1$ and $\tau_d/\tau=10$ is shown for comparison.

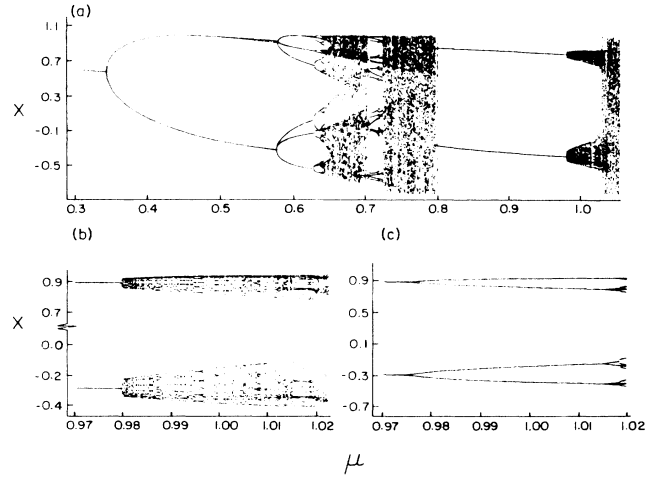

FIG. 8. Numerical bifurcation diagram for $N=100$ ($\tau_d/\tau=0$).

quasiperiodic everywhere on this interval except in a window around $\mu=0.996$, where the two frequency components are locked or entrained together. Figure 9(a) shows the time signal corresponding to this quasiperiodic state. (The time signal for the frequency-locked signal over short-time periods is virtually indistinguishable from the quasiperiodic one.) Fast Fourier transforms of both signals (quasiperiodic and frequency locked) are shown in Figs. 9(b) and 9(c). It is the spectra which allow one to distinguish between the two, since the quasiperiodic one is characterized by the presence of sidebands around each peak. These sidebands can be related to the difference between the irrational ratio of the two frequencies and the nearest rational number corresponding to a frequency-locked situation. For the frequency-locked region the frequencies are in the exact ratio $\frac{11}{2}$. This does not, however, rule out the possibility of narrower frequency-locked windows around the ratio $\frac{11}{2}$ (e.g., the ratio $\frac{23}{4}$), which would not show up in our bifurcation diagram because of the limited resolution used to compute it. A more exhaustive analysis of this quasiperiodic solution is now under investigation.

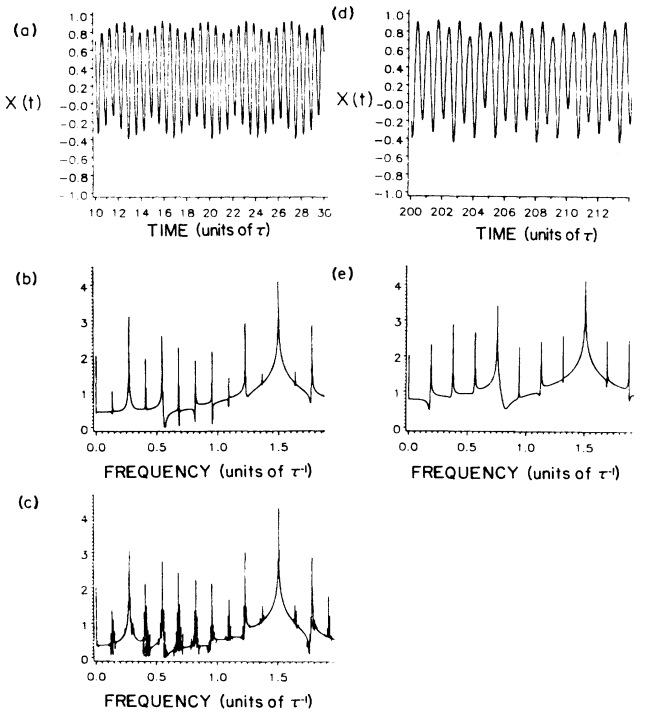

FIG. 9. (a) Time signal of the quasiperiodic waveform obtained for $N=100$ and $\mu=1.01$; (b) fast Fourier transform (FFT) of the frequency-locked signal; (c) FFT of the quasiperiodic waveform; (d) time signal of the $^2P16$ waveform for $\mu=1.017$; (e) FFT of the $^2P16$ waveform.

IV. DISCUSSION

The dynamical evolution of the solution in the general case defined by an Nth-order equation with delay can be analyzed as a function of the two time-related parameters τ_d/τ and N in addition to μ, the parameter controlling the nonlinearity. This problem can, however, be analyzed in terms of two limiting or "pure" cases. The first one corresponds to $N=1$ with $\tau_d\neq 0$ and was the most thoroughly studied in the past.[10] The second, introduced in this paper, is characterized by $N\geq 3$ with $\tau_d=0$.

In fact, the analysis of the "mixed" situation defined by $N>1$ with $\tau_d\neq 0$ (as shown in Fig. 7 for $N=8$) reveals that the corresponding bifurcation diagrams can be closely associated with an equivalent pure case diagram. In other words, no more information on the dynamical evolution of the system is obtained by studying the so-called mixed case. The reason for this can be understood by considering the similarity existing between the two pure cases themselves. Indeed, it is possible to establish a direct relationship between the Nth-order differential equation (DE) and the first-order differential-delay equation (DDE). This correspondence appears very clearly in the linear-stability analyses (LSA's) of the fixed points of both equations. In fact, the LSA's show that as N (or τ_d/τ) is increased the self-oscillation threshold μ^* decreases toward the discrete model value ($\mu=0.32\ldots$). Thus, from the two relationships (N versus μ^*) and (τ_d/τ versus μ^*), it is therefore possible to establish a correspondence between N and τ_d/τ. Figure 10 shows a log-log plot of τ_d/τ as a function of N. One can see that for large N the slope approaches $\frac{1}{2}$, i.e., that τ_d/τ grows as the square root of N.

The correspondence between the first-order DDE and the Nth-order DE is not restricted to the fixed point stability and can be readily extended to the subsequent bifurcations—whether or not they lead to chaos as μ is increased. Such a correspondence is better established by recalling that typical practical values of N correspond to relatively small values of the ratio τ_d/τ. (Notice in Fig. 10 that the square-root relationship previously discussed is an upper limit for τ_d/τ). This is worth noting since most of the previous experimental results from hybrid bistable devices were obtained for relatively large values

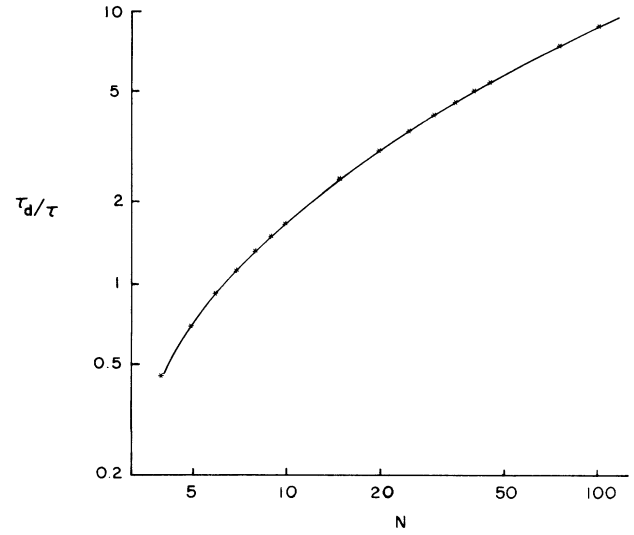

FIG. 10. Correspondence between the Nth-order differential equation and the first-order differential-delay equation. To obtain this plot the thresholds of self-oscillation μ^* were first calculated for some values of N from the LSA of the Nth-order equation without delay. Then the ratios τ_d/τ corresponding to these values of μ^* were computed from the LSA of the first-order equation.

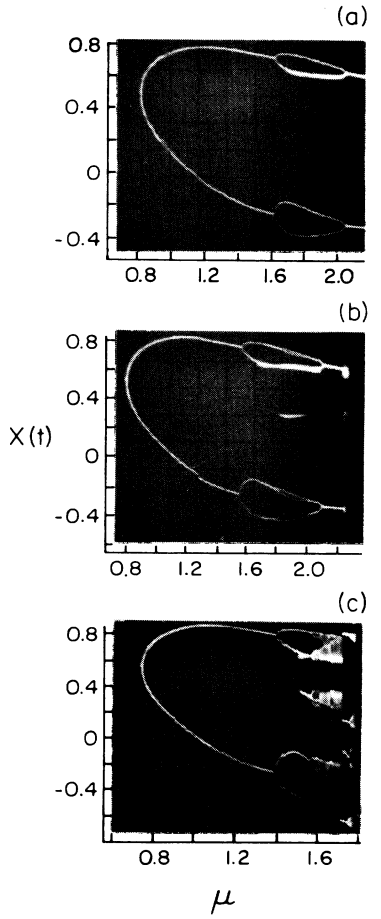

FIG. 11. Experimental bifurcation diagrams for $N=1$ and τ_d/τ around unity: (a) $\tau_d/\tau=1.04$; (b) $\tau_d/\tau=1.12$; (c) $\tau_d/\tau=1.34$.

of τ_d/τ (typically $\tau_d/\tau \geq 10$). Few authors, however, analyzed the situation characterized by a delay smaller or equal to the response time of the system. Although the first-order delay equation studied by these authors [Refs. 10(b) and 10(c)] was slightly different from ours (as their transmission curve maximum was swept along with the parameter controlling the nonlinearity) such a phenomenon as the period bubbling of the $P2$ solution was observed [Ref. 10(b)] or predicted [Ref. 10(c)] for τ_d/τ around unity. We performed both numerically and experimentally an exhaustive analysis of our system for $N=1$ and τ_d/τ around unity. Three typical experimental bifurcation diagrams are shown in Fig. 11. The similarity between these diagrams and those obtained for $N=8$, 9, and 13 (Fig. 3) in the Nth-order case without delay is quite obvious. In fact, a sequence of diagrams similar to that shown in Fig. 3 is obtained for the first-order delayed system as τ_d/τ (instead of N) is increased. For instance, the $P3$ waveforms which disappear for $N>28$ in the Nth-order case also disappear in the first-order delayed case for $\tau_d/\tau \gtrsim 2.5$. Moreover, the position of the period-doubling bifurcations and the exact pitchforklike shape of the solutions in both systems become more and more similar to each other and tend toward those predicted by the discrete model. For instance, the diagram obtained for $N=100$ fits exactly that obtained for $\tau_d/\tau=8.9$ over the periodic region. In the chaotic region such a comparison naturally becomes obsolete because the dimensions of the attractors rapidly become too large to be compared on the basis of a simple one-dimensional bifurcation diagram. This is why we are now in the process of calculating the dimensions of the attractors of both systems in order to compare them as they grow in complexity. In the case of the first-order DDE it is the ratio τ_d/τ which determines the degree of complexity of the solution even though, strictly speaking, the phase-space dimension always remains infinite. In the Nth-order case the phase-space dimension is finite and equal to $N \equiv \tau/\tau_i$ and the asymptotic situation $N \to \infty$, which implies that $\tau_i \to 0$ in order for τ to remain finite, corresponds to a system composed of an infinite number of infinitely fast components. It is therefore an interesting matter to precisely establish how the finite-dimensional Nth-order equation could be used to model the infinite-dimensional first-order delayed equation.

ACKNOWLEDGMENT

This work was supported by the Natural Sciences and Engineering Research Council of Canada.

[1]K. Ikeda, Opt. Commun. **30**, 257 (1979).
[2]M. Leberre, E. Ressayre, A. Tallet, and H. M. Gibbs, Phys. Rev. Lett. **56**, 274 (1986).
[3]R. Vallée, P. Dubois, M. Coté, and C. Delisle, Phys. Rev. A **36**, 1327 (1987).
[4]J. Y. Gao, L. M. Narducci, L. S. Schulman, M. Squicciarini, and J. M. Yuan, Phys. Rev. A **28**, 2910 (1983).
[5]R. Vallée and C. Delisle, IEEE J. Quantum Electron. **QE-21**, 1423 (1985).
[6]J. Stoer and R. Bulirsch, *Introduction to Numerical Analysis* (Springer-Verlag, New York, 1980), p. 404.
[7]R. Vallée, C. Delisle, and J. Chrostowski, Phys. Rev. A **30**, 336 (1984).
[8]M. Bier and T. C. Bountis, Phys. Lett. **104A**, 239 (1984).
[9]R. Vallée and C. Delisle, Phys. Rev. A **34**, 309 (1986).
[10]See, for example: (a) F. A. Hopf, D. L. Kaplan, H. M. Gibbs, and R. L. Shoemaker, Phys. Rev. A **25**, 2172 (1982); (b) M. Okada and K. Takizawa, IEEE J. Quantum Electron. **QE-17**, 2135 (1981); (c) J. Y. Gao, J. M. Yuan, and L. M. Narducci, Opt. Commun. **44**, 201 (1983); (d) J. Chrostowski, R. Vallée, and C. Delisle, Can. J. Phys. **61**, 1143 (1983).

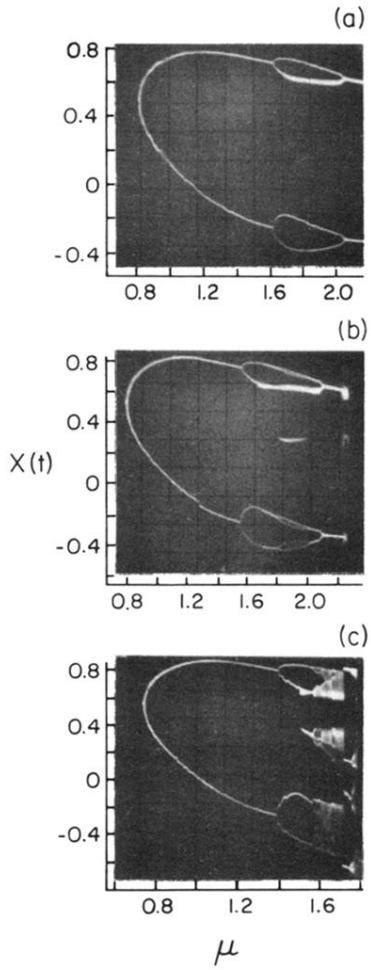

FIG. 11. Experimental bifurcation diagrams for $N=1$ and τ_d/τ around unity: (a) $\tau_d/\tau=1.04$; (b) $\tau_d/\tau=1.12$; (c) $\tau_d/\tau=1.34$.

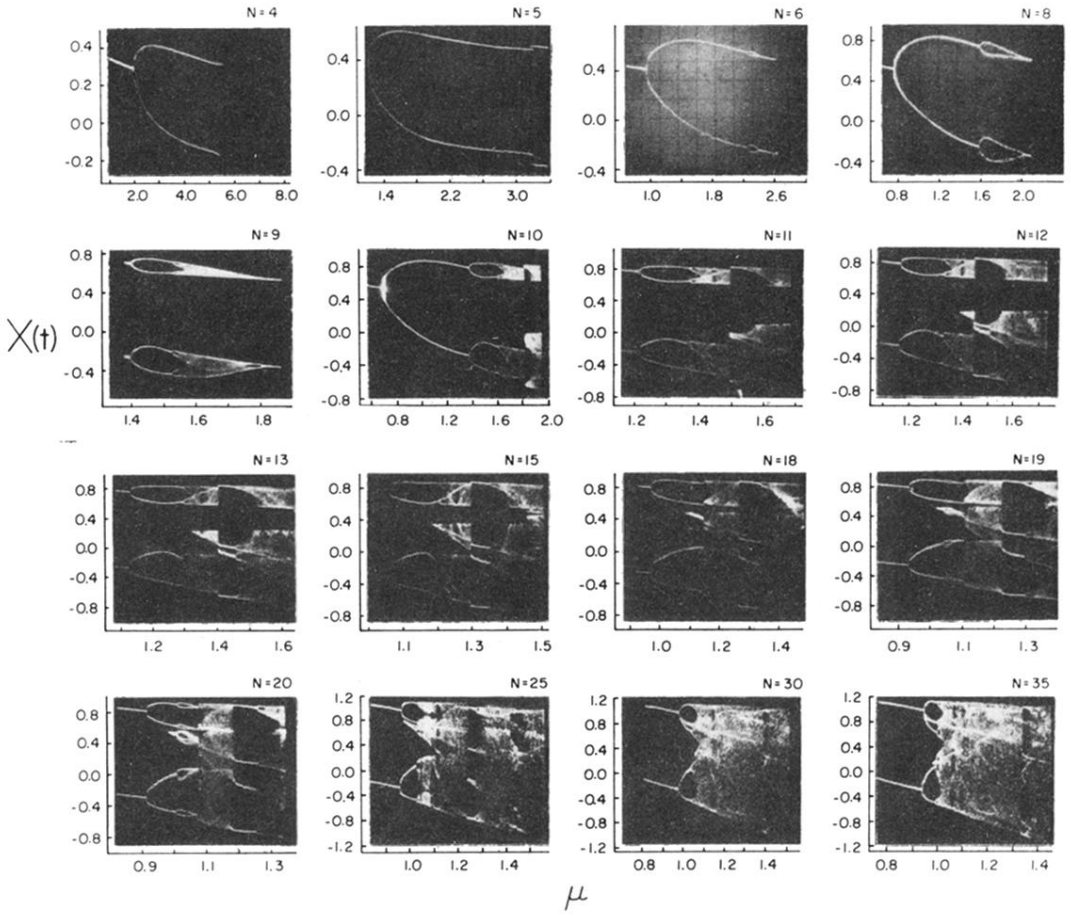

FIG. 3. Experimental bifurcation diagrams.

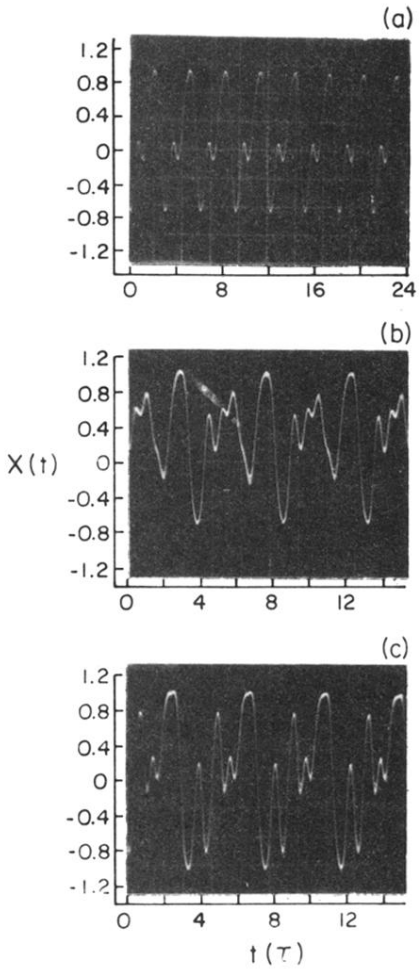

FIG. 4. Periodic waveforms: (a) $P3$ as observed for $N=15$ and $\mu\approx 1.35$; (b) $P5$ for $N=35$ and $\mu=1.07$; (c) $P5$ for $N=35$ and $\mu=1.33$.

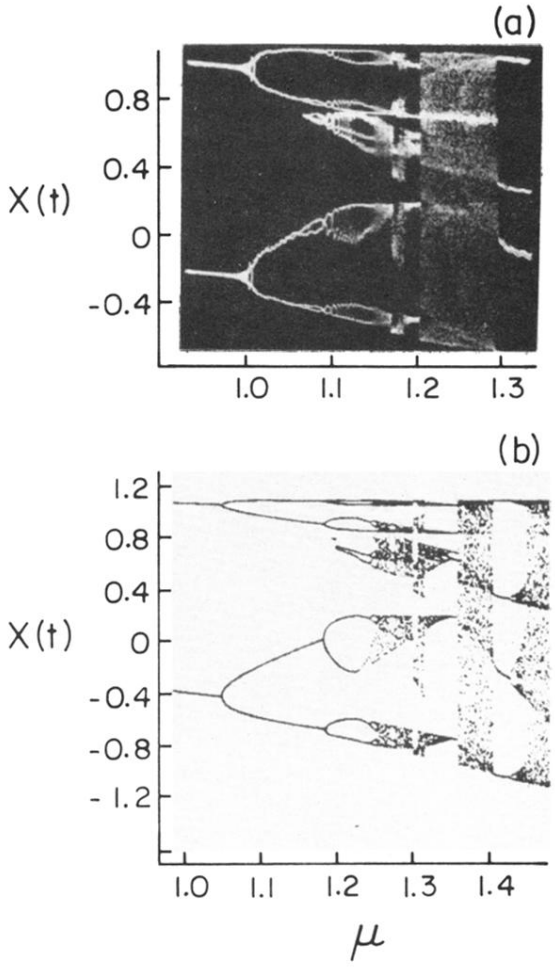

FIG. 6. Comparison between the experimental (a) and the numerical (b) bifurcation diagrams obtained for $N=20$ using the experimental values of τ_i in the computation.